Synthesis of Template-Free CNTS Nanostructures by Hydrothermal Method: Investigating Structural, Photocatalytic, Antibacterial and Electrochemical Properties

S. Manjula[1,], K. Mohanraj[2,] and G. Sivakumar[3,*,]

[1]Department of Physics, Annamalai University, Annamalai Nagar-608002, India
[2]Department of Physics, School of Basic and Applied Sciences, Central University of Tamil Nadu, Thiruvarur-610101, India
[3]Centralized Instrumentation and Service Laboratory, Annamalai University, Annamalai Nagar-608002, India

*Corresponding author: E-mail: gsk.csil@gmail.com

In this study, nanoparticles of quaternary chalcogenide Cu_2NiSnS_4 (CNTS) were prepared by a hydrothermal method to evaluate their electrochemical, photocatalytic and antibacterial performances. The samples were synthesized using aqueous solution of thiourea as a sulfur source without any surfactant assistance. The XRD pattern of the synthesized samples exhibited pure phases of Cu_2NiSnS_4 nanoparticles corresponding to the cubic structure along the (111) plane. The average crystallite sizes decreased with increasing thiourea concentrations. FESEM analysis revealed that the optimized sample exhibited nanosheets with bundle-like structures. The oxidation states of quaternary chalcogenide nanoparticles, such as Cu^{2+}, Ni^{2+} and Sn^{4+} were confirmed by XPS technique. The bandgap value of the synthesized sample was estimated at 1.35 eV. The cyclic voltammetry profiles exhibited pseudocapacitive characteristics, whereas the charge-discharge investigation of the CNTS-10 electrode yielded the highest capacitance value of 374 Fg^{-1} under a low scan rate. The degradation efficiency of two different dyes *e.g.* methylene blue (MB) and crystal violet (CV) was investigated by photocatalytic measurements and the optimized sample CNTS-10 exhibited the highest efficiencies of 88% and 82% respectively. The antibacterial activity results clearly showed that a maximum inhibition rate (22 mm for 100 µg/mL) was found for *Vibrio parahaemolyticus* against other pathogenic bacteria.

Keywords: Surfactant-free, Nanosheets, Methylene blue dye, Crystal violet dye, Photocatalytic activity, Antibacterial activities.

INTRODUCTION

Due to the population expansion, the demand for global energy has increased. Industries are trying to solve this problem by producing electricity as an energy source [1,2]. Particular emphasis has been placed on energy conversion and storage device research and development. An increasing amount of effort is going into creating innovative energy storage systems to meet the rising energy demands of consumers, mostly in relation to the use of state-of-the-art products and smart hybrid electric vehicles, as a result of new ideas [3-5]. Initially, batteries were considered energy storage devices but supercapacitors were introduced with a high-power density that exceeds that of dielectric capacitors [6,7].

Supercapacitors are distinguished by their rapid charging, high durability, low cost and long life [8,9]. The performance of a supercapacitor depends on its electrode material, electrolyte and device configuration. Supercapacitors are of two types: (i) electrical double-layer capacitors (EDLCs) and (ii) pseudo-capacitors. The first type of capacitor retains charge through ion adsorption and release, while the second type employs Faradaic reactions. In EDLCs carbon-based electrode materials, such as graphene, carbon nanotubes (CNTs) and graphene derivatives are frequently employed. On the other hand, sulfides, hydroxides and transition metal oxides are utilized extensively in pseudocapacitors [10-13]. Moreover, one major drawback of EDLC materials is their lower specific capacitance, while the pseudocapacitors have higher specific capacitance due to the presence of redox reactions on electrodes that facilitate high charge storage. Excellent pseudocapacitive materials include a variety of nitrogen sulfides, hydroxides, metal oxides and polymers, which are broadly used. Although metal oxides

are the preferred materials for pseudocapacitive behaviour, the low dielectric potential between the electrode and electrolyte limits the fast movement of electrons [14,15].

Subsequently, due to their extraordinary anisotropic, chemical and physical properties, transition metal chalcogenides (MCs) have attracted great interest in the development of improved electrode materials for supercapacitors. Metal chalcogenides (Cu_2XSnS_4) (X = Zn, Co, Mn, Fe and Ni) have found extensive applications in several fields, including fuel and solar cells [16], antibacterial activity [17], gas sensors [18], lithium-ion batteries [19], electrowater splitting [20] and supercapacitors [21]. This is due to mainly their exceptional features, which include improved conductivity, better life cycle, enhanced conductivity, reduced internal resistance and enhanced catal-ytic activity. Cu_2NiSnS_4, a rarely investigated chalcogenide material corresponding to the class of I_2-II-IV-VI_4 quaternary chalcogenides, is an essential material in photovoltaics due to its optimal band gap for visible light absorption [22]. There are only a few observations of Cu_2NiSnS_4-based supercapacitor applications [23,24].

Various methodologies such as solvothermal, hydrothermal and electro-deposition methods [25-27] have been employed to fabricate porous nanostructures with a high surface area. It has been observed that high-quality synthesized nanostructures are employed to enhance electrode performance. The electrode material capacitance value is improved by favourable electrochemical reactions on the surface of the first few atomic layers. The increased surface area of hierarchical micro/nanostructures increases electrochemical reactions. Templates such as surfactants, capping agents and binding agents are frequently used to regulate crystallite size, surface area or morphologies. Surfactants such as poly(vinyl pyrrolidone) (PVP), cetyl triethylammonium bromide (CTAB) and oleic acid (OA) also affect the environment if used in large amounts in industries. Hence, in this context, a template-free synthetic technique is desired [28].

The novelty of this study is that Cu_2NiSnS_4 nanoparticles were produced without the need of templates by following a straightforward hydrothermal technique. The influence of various thiourea (TU) concentrations is characterized by the structural, morphological and optical properties of CNTS nanoparticles. The electrochemical characteristics of the prepared sample were investigated and the results were discussed. In addition, the prepared catalyst was tested using two different dyes under sunlight irradiation in a photovoltaic application. Furthermore, to the best of our knowledge, this is the first report on *Vibrio parahaemolyticus* for antibacterial activity measurements for the zone of inhibition.

EXPERIMENTAL

The primary precursors employed for preparing Cu_2NiSnS_4 (CNTS) nanoparticles were copper chloride dihydrate [$CuCl_2 \cdot 2H_2O$], nickel nitrate hexahydrate [$Ni(NO_3)_2 \cdot 6H_2O$] and tin(IV) chloride dihydrate [$SnCl_2 \cdot 2H_2O$]. Additionally, thiourea was used as a sulfur source. The CNTS nanoparticles were synthesized using deionized water as solvent and ethanol for purification.

Synthesis of CNTS nanoparticles: Surfactant-free CNTS nanoparticles were synthesized by a hydrothermal technique and deionized water was used as solvent. The CNTS nanoparticles were synthesized using 0.34 g of $CuCl_2 \cdot 2H_2O$, 0.29 g of Ni $(NO_3)_2 \cdot 6H_2O$, 0.22 g of $SnCl_2 \cdot 2H_2O$ and 0.30 g of thiourea in a 2:1:1:4 ratio. The above solutions were mixed and stirred for 15 min by maintaining a constant pH ~ 6. Subsequently, the solutions were poured into a stainless-steel autoclave lined with Teflon to undergo heat treatment by maintaining a constant temperature of 210 ºC for 24 h. The autoclave was cooled to room temperature. After the reaction was completed, Whatman filter paper was used to filter the solution to remove impurities and repeatedly washed with ethanol and deionized water to obtain black-coloured precipitates. The final product was dried at 80 ºC for 3 h in a hot air oven. Furthermore, the thiourea (TU) concentration was varied (4, 6, 8 and 10) and the prepared samples were named CNTS-4 (2:1:1:4), CNTS-6 (2:1:1:6), CNTS-8 (2:1:1:8) and CNTS-10 (2:1:1:10) respectively.

Characterization: The crystallinity of the prepared samples was analyzed by using a PANalytical XPertPRO X-ray diffractometer instrument equipped with a monochromatic CuK_α radiation source ($\lambda = 1.5406$ Å). A Carl Zeiss–Sigma-300 field emission scanning electron microscope (FESEM) was used to record the surface morphology images. The chemical composition of the prepared CNTS nanoparticles was determined using an EDAX spectroscopy-coupled FESEM instrument. The transmission electron microscopy (TEM) with Tecnai G^2 20 S-Twin was also used to determine the sample size and shape. Using a micro laser Raman spectrometer, the identification of characterization peaks was measured. An Evolution UV-1800, Shimadzu, spectrometer was used to investigate the optical characteristics and bandgap of the optimized sample. Metrohm Auto lab M204 electrochemical impedance spectroscopy was used to determine the electrochemical properties of CV, GCD and EIS. At various scan rates from 10 to 50 mV s^{-1} and over a voltage range of 0 to 0.5 V, cyclic voltammetry measurements were conducted.

Photocatalytic activity: The photocatalytic activity of CNTS-10 nanoparticles was evaluated using a UV-Vis spectrophotometer to degrade the two dyes *viz.* methylene blue and crystal violet in aqueous solutions. Initially, 0.05 g of CNTS-10 catalyst was added to 100 mL of 10^{-4} mol/L solution of both dyes. A glass beaker containing both the dye solution and the catalyst (CNTS-10) was placed in the dark for 30 min to obtain an equilibrium between the adsorption and desorption of the catalyst. The samples were exposed to sunlight on a bright and sunny day between 11 a.m. and 2 p.m. The photocatalytic degradation was determined by quantifying the absorption of both dye solutions using UV-Vis spectra before and after irradiation at regular intervals. Following the equation, the photocatalytic degradation efficacy was calculated.

$$\text{Efficiency } (\eta\%) = \left(1 - \frac{C}{C_o}\right) \times 100 \qquad (1)$$

where C_o and C are the initial and final concentrations of the dye, respectively.

Antibacterial activity: The antibacterial activity of CNTS-10 nanoparticles was studied against the growth of *Streptococcus pneumoniae*, *Streptococcus pyogenes*, *Klebsiella pneumoniae* and *Vibrio parahaemolyticus* bacterial strains. The pathogenic bacteria were obtained from ATCC in Bangalore, India. Oral pathogens were stored at 4 ºC and subcultured seven times at a 7-day interval for bacteria. Bacterial pathogens were inoculated into Mueller-Hinton Bouillons (MHB) and incubated at 37 ºC for 24 h. After incubation, the turbidity of the MHB broth indicated the growth of bacterial pathogens. The bacterial cultures were individually spread on agar plates and 6 mm wells were made using a cork borer. The sample (CNTS-10) was dissolved in dimethyl sulfoxide (DMSO). Each well was loaded with 25-100 µL of sample and incubated at 28 ± 2 ºC for 24 h. DMSO was used as a negative control and chloramphenicol (5 µL) was used as the positive control. Finally, the zone of inhibition was measured by the antibiotic zone scale.

RESULTS AND DISCUSSION

Structural analysis: The phase purity and crystallite size of the synthesized CNTS nanoparticles were investigated by X-ray diffraction method. The synthesized CNTS nanoparticles with different thiourea concentrations are shown in Fig. 1. The lower concentration of the thiourea sample (CNTS-4) showed diffraction peaks located at 2θ values of 27.66º, 28.39º, 29.26º, 31.71º, 32.70º, 47.80º, 52.69º and 59.33º corresponding to the (100), (111), (102), (103), (006), (220), (111) and (200) planes, respectively [23]. The results showed that the lower concentration synthesized sample belonged to the mixed phase of CNTS. The mixed phase intensities decreased when the thiourea concentration was slightly increased in CNTS-8 sample. The thiourea concentration was further raised to a 10 ratio (CNTS-10) to assist in the observation of pure phase of Cu_2NiSnS_4 nanoparticles and provided a better comparison to the CNTS-4 sample and the characteristic diffraction peaks appearing at 28.32º, 33.48º, 47.81º and 56.15º were associated with the (111), (200), (220) and (311) planes, respectively. The XRD peaks agreed well with JCPDS no. 26-0552 and cubic phase with space group $F\bar{4}3m$ [27]. There were no noticeable impurity peaks in the synthesized sample indicating the excellent purity of the CNTS nanoparticles. These results suggested that a higher concentration of thiourea played an essential part in the formation of pure phases by removing the possibility of secondary phase formation in the final sample. Furthermore, the better crystalline nature of the synthesized sample caused an increase in the diffraction peaks of CNTS nanoparticles, which were sharpened and broadened due to the increase in thiourea concentration (CNTS-10).

The crystallite size (D) was estimated based on the characteristic peaks of CNTS nanoparticles using Debye-Scherrer's formula [29]:

$$D = \frac{0.9 \times \lambda}{\beta \cos\theta} \qquad (2)$$

where θ = diffraction angle, β = full-width half maximum in radians and λ = wavelength of the X-ray.
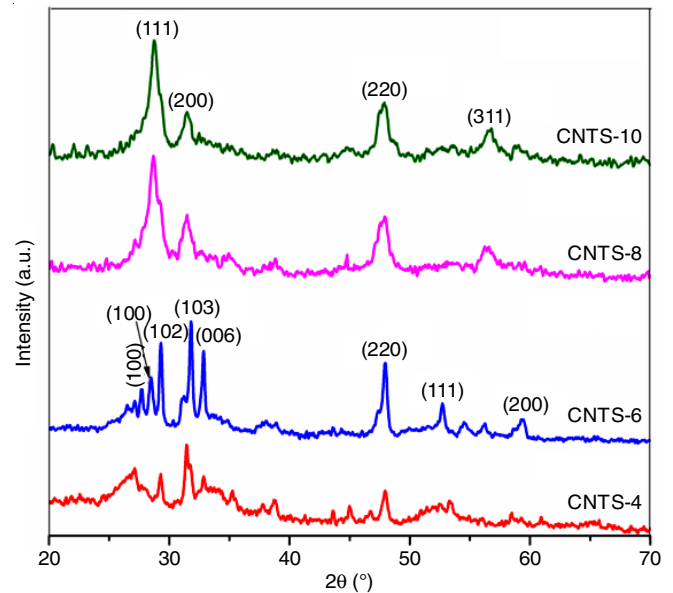

Fig. 1. XRD patterns of CNTS nanoparticles with different thiourea concentrations

The microstrain and dislocation density were calculated by following equations [30]:

$$\delta = \frac{1}{D^2} \qquad (3)$$

$$\varepsilon = \frac{\beta \cos\theta}{4} \qquad (4)$$

The lattice parameter values were estimated based on the interplanar spacing relation:

$$d_{hkl} = \frac{1}{\sqrt{(h^2 + k^2 + l^2)}} \qquad (5)$$

$$n\lambda = 2d_{khl} \sin\theta \qquad (6)$$

The calculated structural parameters for crystallite size (D), microstrain (ε) and dislocation density (δ) values are shown in Table-1. The results revealed that the average crystallite size of the CNTS nanoparticles decreased with the increasing thiourea concentration. The observed results indicated that thiourea influenced the controlling size of prepared samples. Moreover, the dislocation density values were also increased with decreasing crystallite size due to the inversely proportional relationship. The increased microstrain values along with decreased crystallite size were attributed to the CNTS nanoparticles having a more crystalline nature. The lattice parameter values

TABLE-1
STRUCTURAL PARAMETERS - CRYSTALLITE SIZE,
DISLOCATION DENSITY, MICROSTRAIN AND LATTICE
PARAMETER VALUES OF CNTS NANOPARTICLES

Sample	Average crystallite size (D) (nm)	Dislocation density (δ) × 10^4 lines/m²	Micro strain (ε) × 10^{-3}	Lattice constant (a) (Å)
CNTS-4	69	2.1004	0.0311	5.420
CNTS-6	55	3.3058	0.0504	5.422
CNTS-8	37	7.3046	0.0961	5.425
CNTS-10	35	8.1632	0.1050	5.427

slightly decreased with increasing thiourea concentrations and the obtained values were in reasonable accordance with the JCPDS values.

Raman studies: Raman spectrometer was further used to identify the characteristic peaks of the synthesized multi-component phases within the CNTS nanoparticles as shown in Fig. 2. The CNTS-4 sample exhibited a single peak corresponding to the Cu-S stretching vibration at 467 cm^{-1} [24]. The intensity of the Cu-S band decreased while the concentration of thiourea slightly increased which is due to the signature peak of CNTS being formed. The broad peaks of CNTS nanoparticles at 332 cm^{-1} [31] was observed for the sample CNTS-10, which can be due to the A1 symmetric vibrational mode of sulfur atoms. Suryawanshi *et al.* [32] observed the similar results for Cu$_2$NiSnS$_4$ nanoparticles and stated that the high intensity of the Raman peak appeared in the region of 338-328 cm^{-1}. Raman studies showed the A1 symmetry mode of 3 or 4 metals, which was surrounded by a sulfur atom similar to a quaternary system. Furthermore, the absence of possible secondary phases such as Cu$_2$SnS$_3$ (290 and 336 cm^{-1}), Cu$_x$S (475 cm^{-1}) and NiS (244 and 300 cm^{-1}) were not detected in the Raman spectrum [33]. The obtained results suggested that at higher thiourea concentrations (CNTS-10), the CNTS nanoparticles were formed with a pure phase tetragonal kesterite crystal structure without any secondary phases. The CNTS nanoparticles prepared from high thiourea concentration only exhibited the specific peaks in the Raman spectrum. However, only those CNTS prepared with a 2:1:1:10 ratio can result in pure-phase CNTS, as confirmed by Raman and XRD studies.
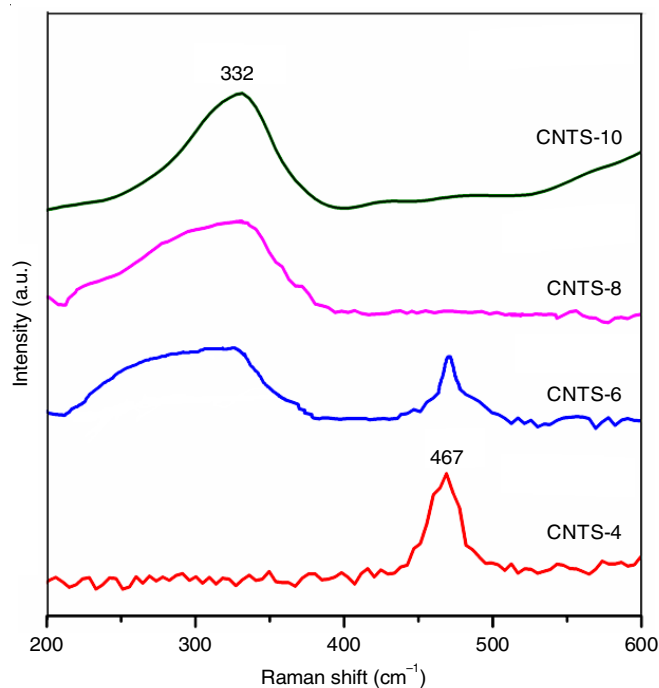

Fig. 2. Raman spectra of CNTS nanoparticles

XPS studies: The oxidation states and chemical information about CuNiSnS$_4$ nanoparticles were determined using XPS technique. The survey scan spectrum of the optimized sample (CNTS-10) is displayed in Fig. 3 and the peaks related to Cu 2p, Ni 2p, O 1s, Sn 3d and S 2p were obtained. High-
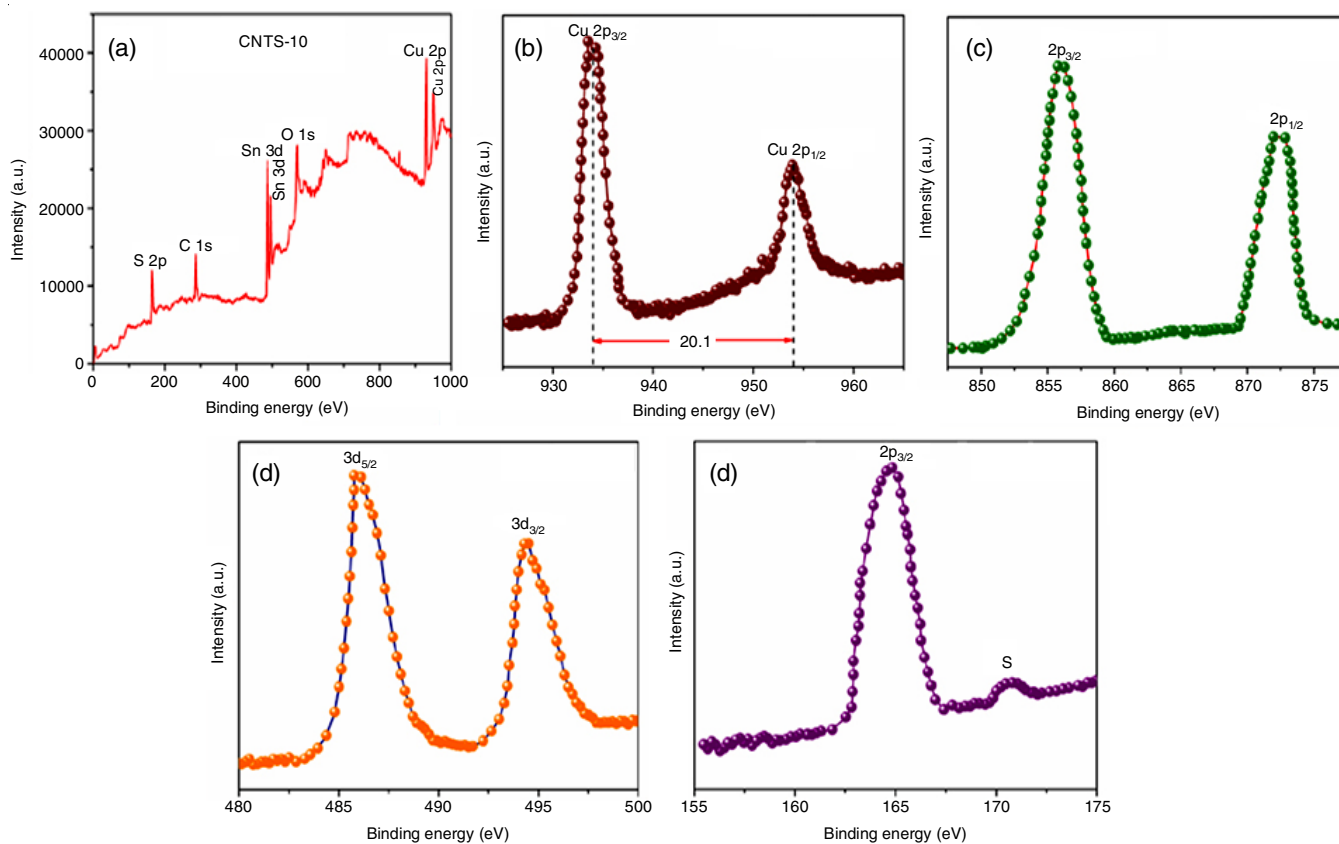

Fig. 3. XPS spectra of CNTS-10 nanoparticles (a) survey scan spectrum, (b) Cu, (c) Ni, (d) Sn, (e) S
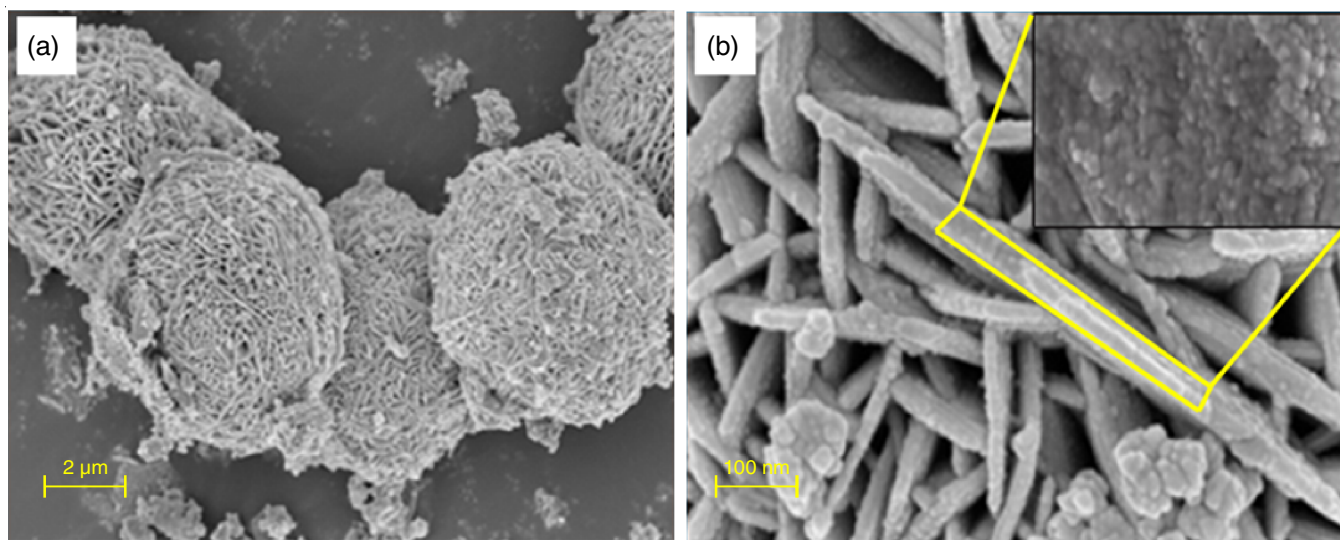
Fig. 4. FESEM images of CNTS-10 nanoparticles, (a,b) low and high magnifications

resolution characteristic peaks were found at 934.4 and 954.5 eV, which matched Cu $2p_{3/2}$ and Cu $2p_{1/2}$, respectively. The distance of approximately 20.1 eV between these two peaks indicates that the oxidation state of copper was +2. At high energies, no satellite peak for Cu $2p_{1/2}$ was found. The observed results in this work are appropriate and comparable with the binding energies of the Cu^{2+} ion, as previously reported [24]. The two apparent sharp binding energies of the Ni $2p_{3/2}$ and Ni $2p_{1/2}$ peaks occurred at 854.2 and 879.3 eV and were associated with the Ni^{2+} state. The spin-orbit split Sn $3d_{5/2}$ and Sn $3d_{3/2}$ peaks, which appeared at 486 and 495 eV, indicated the Sn^{4+} oxidation state. Lower energy peaks for S $2p_{3/2}$ were detected at 164.6 eV and the sulfate peak was located at 170.6 eV [27]. Sulfur species were present in the sulfide and sulfate phases, which could be observed from the S 2p spectrum [34,35]. This was primarily due to the chemisorption of oxygen by the synthesized nanoparticles.

Morphological studies: The morphological features of the CNTS-10 nanoparticles were determined by FESEM and the images are presented in Fig. 4a,b. According to the FESEM images, sample CNTS-10 clearly illustrated the formation of microsphere-like structures which are composed of many freely packed nanosheets. The magnified image revealed that the average thickness of the nanosheets was less than 50 nm. Furthermore, the inset image shows that each nanosheet was formed by small nanoparticles (< 20 nm) and well-distributed large numbers of uniform spherical particles that were closely attached. This kind of structure is preferred for energy storage because sheet-like structures have a larger surface area for high ion diffusion in the electrolyte, which is needed for high-performance supercapacitors.

TEM: The shape and particle size of the CNTS-10 sample were further studied by TEM analysis. Fig. 5a-b shows high and low-resolution TEM images of a spherical structure whose average diameter is about less than 50 nm. The SAED pattern of CNTS-10 nanoparticles is depicted in Fig. 5c and diffraction rings were observed, which revealed the diffuse nature of the polycrystalline nature. In addition, the observed TEM results
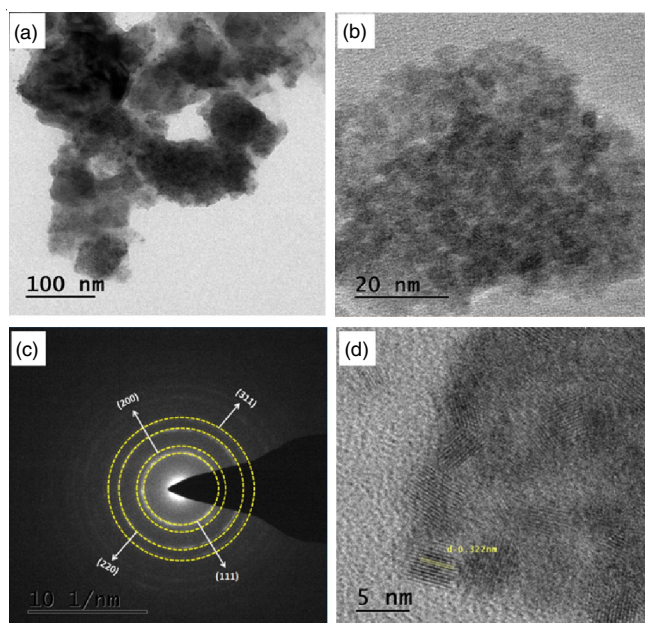

Fig. 5.　TEM images of CNTS-10 nanoparticles (a, b) images, (c) SAED pattern and (d) fringe pattern

confirmed that the synthesized CNTS-10 nanoparticles had a tetragonal kesterite crystal structure, which corresponds very well with the literature reports [21,23]. The lattice fringe pattern of the TEM result is shown in Fig. 5d and the interplanar spacing was approximately 0.322 nm, which was in good accordance with the (111) planes. All of the observed 'd' values and lattice planes corresponded exactly with the XRD data.

Optical properties: The optical properties of the CNTS-10 sample were determined by using UV-Vis spectroscopy and measured in the wavelength range of 200-800 nm. The UV-Vis spectrum of the CNTS-10 sample is shown in Fig. 6a. The measurement revealed a broad optical absorption region and a trace extending to longer wavelengths. The optical bandgap of CNTS-10 nanoparticles for direct bandgap semiconductors was evaluated from the absorbance data using the Tauc relation [36]:
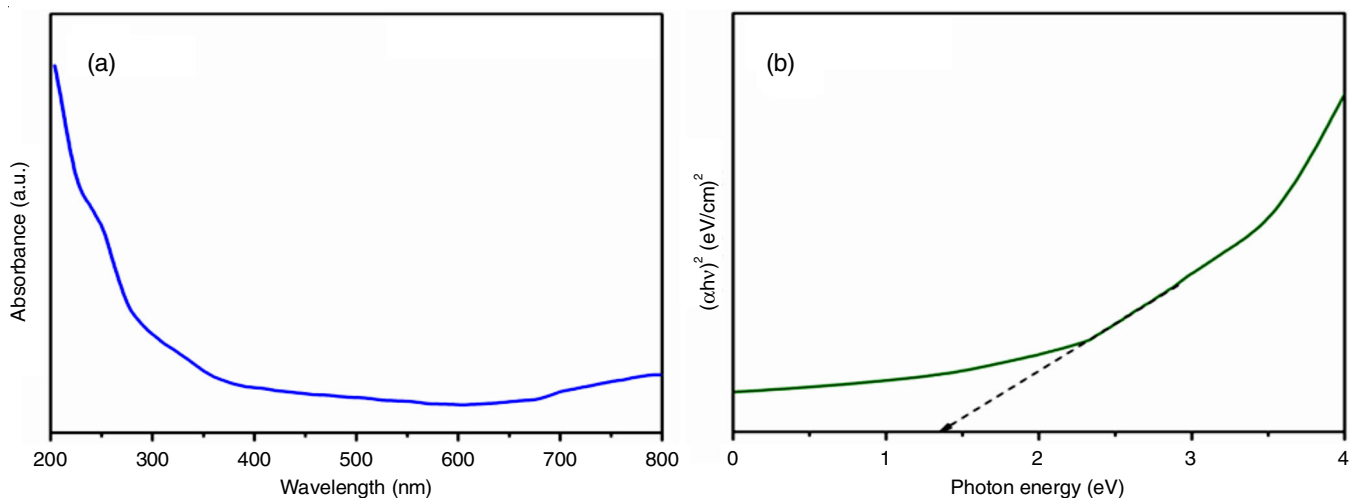
Fig. 6. (a) UV-vis absorbance spectrum and (b) bandgap of CNTS-10 nanoparticles

$$\alpha h\nu = A(h\nu - E_g)^n \tag{7}$$

where $h\nu$ represents the photon energy; E_g represents the optical bandgap of the sample; A represents a constant and n represents 1/2 for a direct bandgap semiconductor. The bandgap of sample CNTS-10 nanoparticles was determined by extending the linear region of the $(\alpha h\nu)^2$ *versus* $(h\nu)$ curve. The bandgap values were calculated by extrapolating linear parts of the plots onto the energy axis. From Fig. 6b, the calculated bandgap value was determined to be approximately 1.35 eV and the corresponding bandgap value was consistent with reported results [30].

Electrochemical analysis: Cyclic voltammetry was used to assess the electrochemical performance of CNTS as a super-capacitor electrode material by using a three-electrode setup (CNTS-10 sample was used as the working electrode, Ag/AgCl as the reference electrode and Pt wire was used as the counter electrode in aqueous 6 M KOH electrolyte). The cyclic voltammetry studies were conducted at various scan rates (10-100 mV/s) and the potential range was between 0 and 0.5 mV. The redox activity of the CNTS electrode was confirmed by two redox peaks illustrated in the crystal violet graph (Fig. 7a). Shifts in the oxidation and reduction peaks were observed at higher positive and lower negative potentials as the scan rate

increased which might be related to the electrode's resistive effect, polarization and rapid ion kinetics. The rising current response confirmed a direct relationship with the scan rate, which revealed enhanced capacitive performance. This result could also signify that the electrode material facilitated ion diffusion and had a large specific area. The fact that faradaic redox processing was well reversible at high specific capacity and low scan rates indicated that the electrode material had a high-rate capability. In the diffusion-controlled process, the obtained redox peaks indicated a linear relationship between the current and scan rate. This was because the distribution of oxidation and reduction during OH diffusion could occur between the electrolyte and the electrode surface of medium, respectively. Franklin *et al.* [24] stated that quaternary chalcogenides improved the contact area of the composite electrode when the Cu_2NiSnS_4 microstructure was properly selected. This higher porosity, conductivity and surface area attracted more ions to the surface electrode, facilitating easy ion transport. As a consequence, the conductivity significantly increased [24].

The specific capacitance (C_s) was evaluated by following relation [37]:
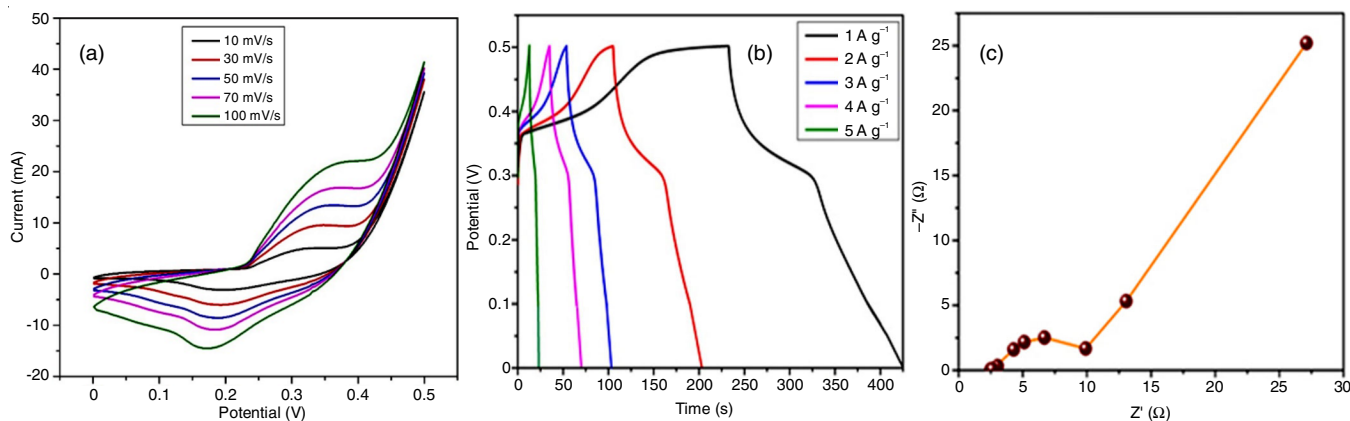
$$C_s \int \frac{I.dv}{mv.\Delta v} \tag{8}$$

Fig. 7. (a) Cyclic voltammetry curves of CNTS-10 electrode, (b) GCD curves of CNTS-10 electrode and (c) Nyquist plot of CNTS-10 nanoparticles

where m represents the mass of active material on the electrode surface; I.dv represents the integrated area under the curve and Δv represents the difference in the potential window (mV/s) with different scan rates. The calculated specific capacitance values were 374, 223, 146, 136 and 121 F g^{-1} for 10, 30, 50, 70 and 100 mVs^{-1}, respectively. The results showed that the specific capacitance values steadily decreased with increasing scan rates, which was clarified by a simple correlation between the scan rate and redox reaction. Due to the timescale limitations, at higher current densities, only the external active surface of the electrode was utilized, whereas, at lower current densities, both the internal and external active surfaces were utilized to promote efficient redox activity [38].

The specific capacitance values of optimized sample CNTS-10 further confirmed the galvanostatic charge-discharge analysis. Fig. 7b depicts the galvanostatic curves of CNTS-10 determined by a potential window of 0-0.5 V with various current densities from 1 to 5 A/g. The GCD results revealed that every curve was non-linear which was deposited from the triangular trend and revealed the redox behaviour of the optimized sample at the surface of electrode. The charge/discharge time length was reduced as the current density increased. In addition, the discharge curves demonstrated the dominance of redox activity at all current densities without a substantial decrease in capacitance, which indicated the suitability of the electrode for practical applications. The specific capacitances of the CNTS-10 electrode were calculated using the following relation [39]:

$$C_s = \frac{I\Delta t}{\Delta V m} \quad (9)$$

where I is the discharge current, ΔV is the potential change during the discharge, m is the mass of active material on the electrode and Δt is the discharge time. The GCD curves delivered specific capacitance values of 360, 344, 270, 240 and 100 F g^{-1} for different current densities at 1, 2, 3, 4 and 5 A g^{-1}, respectively. Based on this study, sample CNTS-10 exhibited

the highest specific capacitance value of 360 F g^{-1} at a low current density. Additionally, the lower capacitance values might be explained by limited electrolyte diffusion at high current and partial insertion reaction at the accessible reaction sites and the corresponding specific capacitance values decreased with increasing current density [40].

Electrochemical impedance spectroscopy (EIS) was applied to examine the charge transfer characteristic of the CNTS-10 electrode. Fig. 7c shows the Nyquist plot of the CNTS-10 electrode. The Nyquist plots showed a half-circle and a straight line at low and high frequencies, respectively. The half-circle obtained at the higher frequency was due to the charge transfer resistance, which indicated rapid ion diffusion during the redox reaction. At lower frequencies, the sloping line represented the Warburg element, indicating the transfer of electrolytes which occurred through a diffusion process and demonstrated its electroactive nature. Furthermore, a nearly vertical line in the low-frequency region was primarily caused by the pseudo-capacitive behaviour.

Photocatalytic activity: The photocatalytic activities of the CNTS-10 sample were tested utilizing the photocatalytic degradation of methylene blue and crystal violet dye solutions under sunlight irradiation and the results are shown in Fig. 8a-b. The strong peaks at 665 nm for methylene blue and 590 nm for crystal violet indicate the maximum absorbance values of the corresponding dye solutions. The dye removal efficiency of the sample was determined by collecting the sample every 10 min. From the absorption spectra, both dye solutions slowly decreased as the sunlight irradiation time indicated the oxidation of dye. The absorption spectra indicated that the characteristic absorption spectra of methylene blue and crystal violet dyes steadily decrease with increasing irradiation time intervals and disappear completely after 70 min. Chen *et al.* [41] stated that the initial concentration of dye increased and more dye molecules were adsorbed on the surface of photocatalyst. The adsorption of O$_2^-$ and OH$^-$ on the photocatalyst was decreased due to the dye molecules that filled a significant number of active
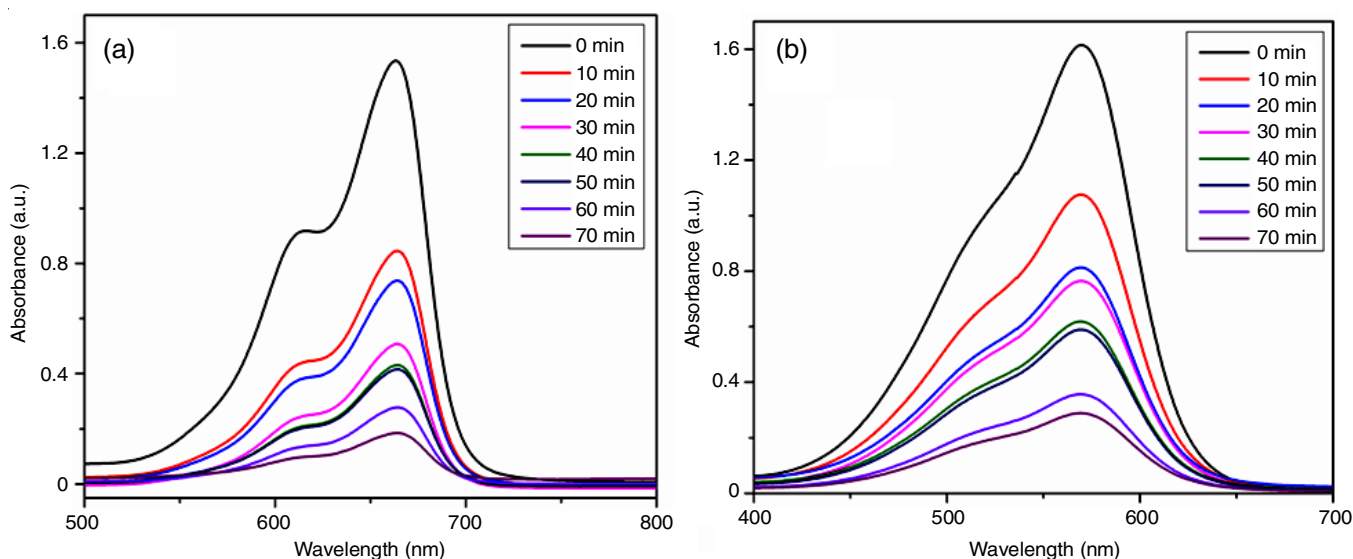

Fig. 8. Time-dependent absorption spectra for different dye solutions containing the CNTS-10 catalyst under visible light illumination; (a) methylene blue dye and (b) crystal violet dye

sites, which lowered radical generation. In addition, photons were inhibited before they reached the photocatalyst surface, reducing photon adsorption by the photocatalyst [41]. The observed results suggested that the methylene blue dye-based CNTS-10 nanoparticles exhibited the highest photocatalytic degradation whereas the degradation rate of crystal violet-based CNTS-10 nanoparticles was very slow under sunlight illumination, which was mostly due to the photosensitization of dye.

The degradation efficiencies of CNTS-10 nanoparticles were investigated by both dye solutions and the results are displayed in Fig. 9a-b. The degradation efficiencies of CNTS-10 sample towards methylene blue and crystal violet dyes were 88% and 82%, respectively. The degradation efficiency of methylene blue dye based CNTS nanoparticles was found to be much more than that of crystal violet dye. The high degradation efficiency is due to the material shape, surface area, morphology and crystallinity, which are the primary factors in the photocatalytic activity. During the photocatalytic process, the molecules of crystal violet or methylene blue are adsorbed on the surface of CNTS-10 nanoparticles. Additionally, crystal violet or methylene blue dye radicals are generated by sunlight. Similarly, CNTS-10 nanoparticles exposed to sunlight can form electron (e^-) – hole (h^+) pairs. This electron-hole can be extracted from the surface of CNTS-10 sample. The subsequent interaction of electrons (e^-) with oxygen molecules (O_2) can lead to the formation of superoxide anion (O_2^-). These super-

oxide anions interact with H^+ and can generate hydroxyl radicals ($OH^\bullet$). Holes (h^+) are capable of oxidizing water molecules (H_2O) and hydroxyl radicals (OH^-). The O_2 and OH radicals are extremely reactive and can destroy crystal violet or methylene blue dye through oxidation. It is well-known that decreasing crystallite size with an increasing surface area of the CNTS-10 catalyst is considered a major strategy to enhance photocatalytic performance. Furthermore, a comparison study between the CNTS nanoparticles and the other catalysts that have been previously reported for photocatalytic degradation of industrial dyes has been built to reflect the validity of the developed CNTS nanoparticles as catalyst for dye degradation, as shown in Table-2. The outcomes demonstrated that in the present work, especially without the use of surfactants, has excellent performance when compared to other catalysts.

Antibacterial activity: Fig. 10 depicts the antibacterial activity of CNTS-10 nanoparticles against various bacteria using the well diffusion agar method. The results indicated that CNTS-10 nanoparticles had excellent antibacterial action against a variety of microorganisms. The diameter of the inhibition zone was proportional to the susceptibility of microorganisms. Four different concentrations of CNTS-10 nanoparticles were used to observe the zone of inhibition. The nanoparticle diffusion inhibited the growth of the bacterial strains *S. pneumoniae*, *S. pyogenes*, *K. pneumoniae* and *V. parahaemolyticus* at different concentrations of 25, 50, 75 and 100 µg/mL, respectively. The results in Table-3 revealed that the growth inhibition increased
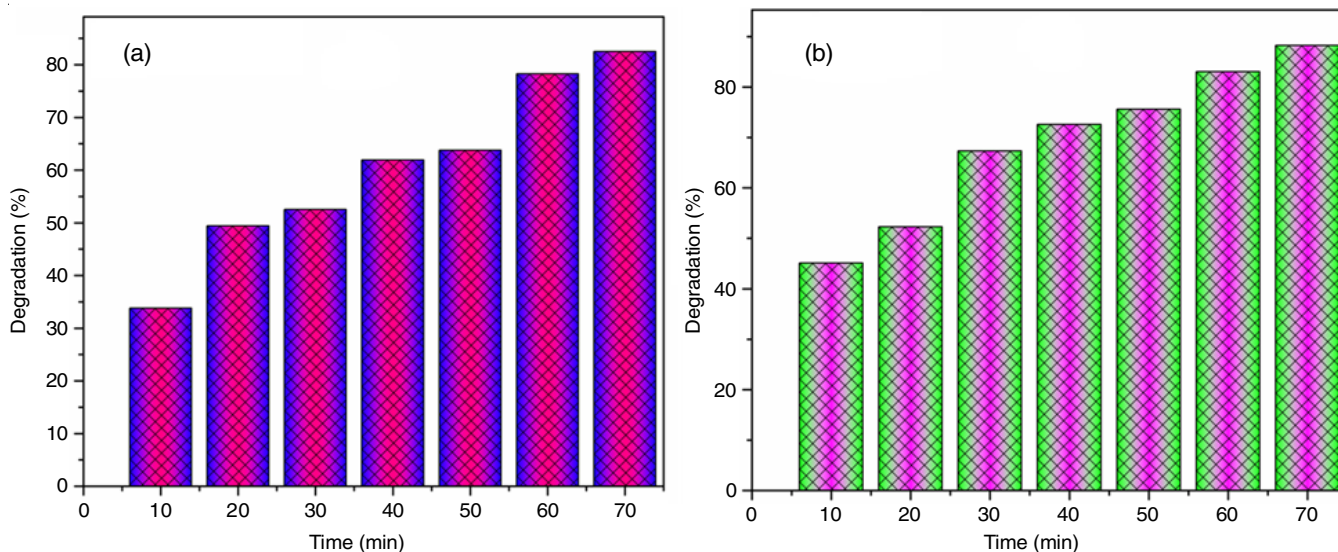

Fig. 9. Degradation efficiencies of CNTS-10 nanoparticles using two different dyes (a) crystal violet dye and (b) methylene blue dye

TABLE-2
PHOTOCATALYTIC DEGRADATION OF INDUSTRIAL DYES USING DIFFERENT NANOMATERIALS

Nanomaterials	Surfactants	Bandgap (eV)	Model industrial dye	Removal efficiency	Time (min)	Ref.
Cu_2SnS_3	Ethanol	2.2	Methylene blue	90%	180	[42]
Cu_2FeSnS_4	Thioglycolic acid	1.40	MR	74%	180	[43]
Cu_2NiSnS_4	Ethylenediamine	1.41	Methylene blue	84%	100	[44]
Cu_2ZnSnS_4	Oleyl amine	1.50	Rhodamine B	60%	240	[45]
CTS/RGO	Polyvinylpyrrolidone	1.31	Rhodamine B	87%	210	[46]
Cu_2NiSnS_4	–	1.35	Methylene blue	88%	70	This study
Cu_2NiSnS_4	–	1.35	Crystal violet	82%	70	This study

TABLE-3
ANTIBACTERIAL ACTIVITIES OF THE CNTS SAMPLE

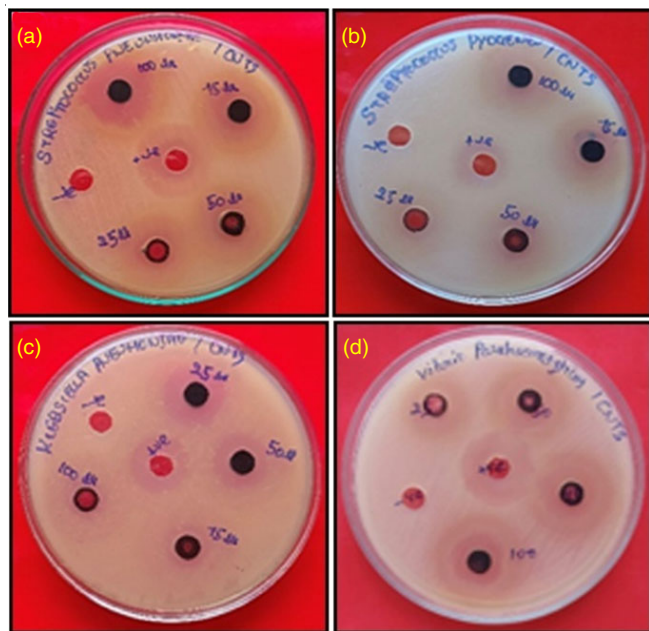| Test organisms	Zone of inhibition (mm)					
	25 µL	50 µL	75 µL	100 µL	Positive control	Negative control
Streptococcus pneumoniae	10 mm	12 mm	14 mm	16 mm	26 mm	–
Streptococcus pyogenes	8 mm	10 mm	12 mm	14 mm	26 mm	–
Klebsiella pneumoniae	14 mm	16 mm	18 mm	20 mm	26 mm	–
Vibrio parahaemolyticus	16 mm	18 mm	20 mm	22 mm	29 mm	–

Fig. 10. Antibacterial activity of the CNTS-10 nanoparticles (a) *Streptococcus pneumoniae*, (b) *Streptococcus pyogenes* (c), *Klebsiella pneumoniae* and (d) *Vibrio parahaemolyticus*

with increasing concentrations of CNTS-10 nanoparticles. The maximum zones of inhibition of CNTS-10 nanoparticles against *V. parahaemolyticus* bacteria at 25, 50, 75 and 100 µg/mL were 16, 18, 20 and 22 mm, respectively. The size of the inhibition zone varied depending on the type of bacteria, particle size and nanoparticle concentration. The lower incubation zone was due to the CNTS-10 nanoparticles, which produced a quick loss in bacterial cell membrane integrity as well as the production of reactive oxygen species (ROS), which formed superoxide species and contributed to biomolecule destruction. Based on this study, the prepared CNTS-10 nanoparticles exhibited a smaller particle size and higher surface area. They had a greater probability of entering into contact with *V. parahaemolyticus* and enhanced the antibacterial activity.

Conclusion

Quaternary chalcogenide Cu_2NiSnS_4 (CNTS) nanosheets were successfully prepared by a hydrothermal method without adding templates. The XRD patterns revealed that the single phase of the CNTS nanoparticles was obtained at higher concentrations of thiourea and the average crystallite size was decreased. Raman spectroscopic studies confirmed the formation of the single pure phase of Cu_2NiSnS_4 without any secondary phase. FESEM images of the optimized sample exhibited a nanosheet-like structure. The optical properties of the prepared sample showed broad absorption in the visible region and a bandgap value of 1.35 eV. The electrochemical measurements indicated that the CNTS-10 nanoparticles showed a high specific capacitance with a pseudocapacitive nature. For the photocatalytic measurements, the degradation efficiencies of CNTS-10 nanoparticles against methylene blue and crystal violet dyes were 88% and 82%, respectively. The CNTS nanoparticles showed significant antibacterial activity in terms of zone of inhabitation against *Vibrio parahaemolyticus*. The investigations suggested that this material could be used in future energy storage and biological applications.

CONFLICT OF INTEREST

The authors declare that there is no conflict of interests regarding the publication of this article.

REFERENCES

1. C. Huang, Y. He, X. Wu, R. Ge, X. Zu, S. Li and L. Qiao, *J. Power Sources*, **456**, 228023 (2020);
   https://doi.org/10.1016/j.jpowsour.2020.228023
2. Y. Liu, Q. Wu, L. Liu, P. Manasa, L. Kang and F. Ran, *J. Mater. Chem. A*, **8**, 8218 (2020);
   https://doi.org/10.1039/D0TA01490G
3. J. Mitali, S. Dhinakaran and A.A. Mohamad, *Energy Storage Saving*, **1**, 166 (2022);
   https://doi.org/10.1016/j.enss.2022.07.002
4. M. Farghali, A.I. Osman, I.M.A. Mohamed, Z. Chen, L. Chen, I. Ihara, P.-S. Yap and D.W. Rooney, *Environ. Chem. Lett.*, **21**, 2003 (2023);
   https://doi.org/10.1007/s10311-023-01591-5
5. X. Shi, S. Zhang, X. Chen, T. Tang and E. Mijowska, *Carbon*, **157**, 55 (2020);
   https://doi.org/10.1016/j.carbon.2019.10.004
6. C. Yuan, J. Li, L. Hou, X. Zhang, L. Shen and X.W.D. Lou. *Adv. Funct. Mater.*, **22**, 4592 (2012);
   https://doi.org/10.1002/adfm.201200994
7. H. Wang, Q. Gao and L. Jiang, *Small*, **7**, 2454 (2011);
   https://doi.org/10.1002/smll.201100534
8. B.E. Conway, V. Birss and J. Wojtowicz, *J. Power Sources*, **66**, 1 (1997);
   https://doi.org/10.1016/S0378-7753(96)02474-3
9. R. Kötz and M. Carlen, *Electrochim. Acta*, **45**, 2483 (2000);
   https://doi.org/10.1016/S0013-4686(00)00354-6
10. P.C. Gao, W.Y. Tsai, B. Daffos, P.L. Taberna, C.R. Pérez, Y. Gogotsi, P. Simon and F. Favier, *Nano Energy*, **12**, 97 (2015);
    https://doi.org/10.1016/j.nanoen.2014.12.017
11. Y. He, W. Chen, C. Gao, J. Zhou, X. Li and E. Xie, *Nanoscale*, **5**, 8799 (2013);
    https://doi.org/10.1039/c3nr02157b

12. D. Chen, K. Jiang, T. Huang and G. Shen, *Adv. Mater.*, **32**, 1901806 (2020);
https://doi.org/10.1002/adma.201901806

13. M. Härmas, R. Palm, T. Thomberg, R. Härmas, M. Koppel, M. Paalo, I. Tallo, T. Romann, A. Jänes and E. Lust, *J. Appl. Electrochem.*, **50**, 15 (2020);
https://doi.org/10.1007/s10800-019-01364-5

14. X. Wu, J. He, M. Zhang, Z. Liu, S. Zhang, Y. Zhao, T. Li, F. Zhang, Z. Peng, N. Cheng, J. Zhang, X. Wen, Y. Xie, H. Tian, L. Cao, L. Bi, Y. Du, H. Zhang, J. Cheng, X. An, H. Lei, H. Shen, J. Gan, X. Zu, S. Li and L. Qiao, *Nano Energy*, **67**, 104247 (2020);
https://doi.org/10.1016/j.nanoen.2019.104247

15. B. Khan, F. Raziq, M. Bilal Faheem, M. Umar Farooq and S. Hussain, F. Ali, A. Ullah, A. Mavlonov, Y. Zhao, Z. Liu, H. Tian, H. Shen, X. Zu, S. Li, H. Xiao, X. Xiang and L. Qiao, *J. Hazard. Mater.*, **381**, 120972 (2020);
https://doi.org/10.1016/j.jhazmat.2019.120972

16. A.C. Lokhande, R.B.V. Chalapathy, M. He, E. Jo, M. Gang, S.A. Pawar, C.D. Lokhande and J.H. Kim, *Sol. Energy Mater Sol. Cells*, **153**, 84 (2016);
https://doi.org/10.1016/j.solmat.2016.04.003

17. A.C. Lokhande, A.A. Yadav, J. Lee, M. He, S.J. Patil, V.C. Lokhande, C.D. Lokhande and J.H. Kim, *J. Alloys Compd.*, **709**, 92 (2017);
https://doi.org/10.1016/j.jallcom.2017.03.135

18. H. Wu, D. Liu, H. Zhang, C. Wei, B. Zeng, J. Shi and S. Yang, *Carbon*, **50**, 4847 (2012);
https://doi.org/10.1016/j.carbon.2012.06.011

19. V. Maheskumar, P. Gnanaprakasam, T. Selvaraju and B. Vidhya, *Int. J. Hydrogen*, **43**, 3967 (2018);
https://doi.org/10.1016/j.ijhydene.2017.07.194

20. Q. Tang, H. Shen, H. Yao, W. Wang, Y. Jiang and C. Zheng, *Ceramics Int.*, **42**, 10452 (2016);
https://doi.org/10.1016/j.ceramint.2016.03.194

21. C. Wang, H. Tian, J. Jiang, T. Zhou, Q. Zeng, X. He, P. Huang and Y. Yao, *ACS Appl. Mater. Interfaces*, **9,** 26038 (2017);
https://doi.org/10.1021/acsami.7b07190

22. J. Rajavedhanayagam, V. Murugadoss, D.K. Maurya and S. Angaiah, ES *Energy Environ.*, **18**, 65 (2022);
https://doi.org/10.30919/esee8c753

23. S. Sarkar, P. Howli, U.K. Ghorai, B. Das, M. Samanta, N.S. Das and K.K. Chattopadhyay, *CrystEngComm*, **20**, 1443 (2018);
https://doi.org/10.1039/C7CE02101A

24. M. Isacfranklin, R. Yuvakkumar, G. Ravi, S.I. Hong, M. Thambidurai, F. Shini, C. Dang and D. Velauthapillai, *Sci. Rep.*, **10**, 19198 (2020);
https://doi.org/10.1038/s41598-020-75879-9

25. T.X. Wang, Y.G. Li, H.R. Liu, H. Li and S.X. Chen, *Mater. Lett.*, **124**, 148 (2014);
https://doi.org/10.1016/j.matlet.2014.03.044

26. H.J. Chen, S.W. Fu, T.C. Tsai and C.F. Shih, *Mater. Lett.*, **166**, 215 (2016);
https://doi.org/10.1016/j.matlet.2015.12.082

27. S. Sarkar, P. Howli, B. Das, N.S. Das, M. Samanta, G.C. Das and K.K. Chattopadhyay, *ACS Appl. Mater. Interfaces*, **9**, 22652 (2017);
https://doi.org/10.1021/acsami.7b00437

28. J. Wang, P. Zhang, X. Song and L. Gao, *RSC Adv.*, **4**, 27805 (2014);
https://doi.org/10.1039/C4RA03444A

29. S. Manjula, A. Sarathkumar and G. Sivakumar, *J. Nano Res.*, **79**, 25 (2023);
https://doi.org/10.4028/p-b6b546

30. S. Dridi, N. Bitri and M. Abaab, *Mater. Lett.*, **204**, 61 (2017);
https://doi.org/10.1016/j.matlet.2017.06.028

31. M.A. Abed, N.A. Bakr and J. Al-Zanganawee, *Chalcogenide Lett.*, **17**, 179 (2020).

32. M.P. Suryawanshi, G.L. Agawane, S.M. Bhosale, S.W. Shin, P.S. Patil, J.H. Kim and A.V. Moholkar, *Mater. Technol.*, **28**, 98 (2013);
https://doi.org/10.1179/1753555712Y.0000000038

33. P.R. Ghediya, Y.M. Palan, D.P. Bhangadiya, I.I. Nakani, T.K. Chaudhuri, K. Joshi, C.K. Sumesh and J. Ray, *Mater. Today Commun.*, **28**, 102697 (2021);
https://doi.org/10.1016/j.mtcomm.2021.102697

34. M. Aono, K. Yoshitake and H. Miyazaki, *Phys. Status Solidi C*, **10** 1058 (2013);
https://doi.org/10.1002/pssc.201200796

35. C. Xiao, K. Li, J. Zhang, W. Tong, Y. Liu, Z. Li, P, Huang, B. Pan, H. Sud and Y. Xie, *Mater. Horiz.* **1**, 81 (2014);
https://doi.org/10.1039/C3MH00091E

36. H. Nishi, T. Nagano, S. Kuwabata and T. Torimoto, *Phys. Chem. Chem. Phys.*, **16**, 672 (2014);
https://doi.org/10.1039/C3CP53946F

37. Y. Li, Q. Wang, J. Shao, K. Li and W. Zhao, *ChemistrySelect*, **5**, 5501 (2020);
https://doi.org/10.1002/slct.202001254

38. A.C. Lokhande, A. Patil, A. Shelke, P.T. Babar, M.G. Gang, V.C. Lokhande, D.S. Dhawale, C.D. Lokhande and J.H. Kim, *Electrochim. Acta*, **284**, 80 (2018);
https://doi.org/10.1016/j.electacta.2018.07.170

39. S. Dang, Z. Wang, W. Jia, Y. Cao and J. Zhang, *Mater. Res. Bull.*, **116**, 117 (2019);
https://doi.org/10.1016/j.materresbull.2019.04.023

40. Y. Feng, W. Liu, Y. Wang, W. Gao, J. Li, K. Liu, X. Wang and J. Jiang, *J. Power Sources*, **458**, 228005 (2020);
https://doi.org/10.1016/j.jpowsour.2020.228005

41. X. Chen, Z. Wu, D. Liu and Z. Gao, *Nanoscale Res Lett.*, **12**, 143 (2017);
https://doi.org/10.1186/s11671-017-1904-4

42. A.R. Machale, S.A. Phaltane, H.D. Shelke and L.D. Kadam, *Mater. Today Proc.*, **43**, 2768 (2021);
https://doi.org/10.1016/j.matpr.2020.07.481

43. M.B. Zaman, T. Chandel and R. Poolla, *Mater. Res. Express*, **6**, 075058 (2019);
https://doi.org/10.1088/2053-1591/ab1797

44. H. Guan, X. Gu and X. Chen, *Chalcogenide Lett.*, **15**, 345 (2018).

45. X. Yu, A. Shavel, X. An, Z. Luo and A. Cabot, *J. Am. Chem. Soc.*, **136**, 9236 (2014);
https://doi.org/10.1021/ja502076b

46. S. Yao, L. Xu, Q. Gao, X. Wang, N. Kong, W. Li, J. Wang, G. Li and X. Pu, *J. Alloys Compd.*, **704**, 469 (2017);
https://doi.org/10.1016/j.jallcom.2017.02.069